Highly accurate and efficient potential for bcc iron assisted by artificial neural networks

Meng Zhang [1,*] Koki Hibi,[2] and Junya Inoue [1,2,3,†]

[1]*Institute of Industrial Science, The University of Tokyo, 5-1-5 Kashiwanoha, Kashiwa, Chiba 277–8574, Japan*

[2]*Department of Materials Engineering, The University of Tokyo, 7-3-1 Hongo, Bunkyo, Tokyo 113–8656, Japan*

[3]*Research Center for Advanced Science and Technology, The University of Tokyo, 4-6-1 Komaba, Meguro, Tokyo 153–8904, Japan*

(Received 11 February 2024; revised 3 June 2024; accepted 30 July 2024; published 26 August 2024; corrected 20 September 2024)

Atomic forces and energies, calculated by interatomic potential, are fundamental components of molecular dynamics (MD) and Monte Carlo (MC) simulations. Compared with traditional potentials, machine-learning (ML) potentials trained by using extensive density-functional theory databases exhibit high accuracy in predicting physical and chemical properties of materials, but their transferability often faces constraints. To address this limitation, physically informed neural network (PINN) potentials have been developed. These models synergistically combine the strengths of ML with physics-based bond-order interatomic potentials, aiming for both improved accuracy and broader applicability. However, a major limitation remains: the low performance of PINN potentials, hindering large-scale simulations. This work introduces a potential framework by incorporating an artificial neural network (ANN) into typical potential functions, which not only improves the transferability compared with the ANN potential, but also significantly improves the performance of ML potentials. The developed ANN assistant potential for body-centered cubic (bcc) iron demonstrates exceptional accuracy in property predictions while boasting remarkable computational efficiency. Its performance utilizing a single graphics processing unit (GPU) card overcomes both 12-message passing interface central processing unit -only ML potential and GPU-accelerated ML potential by achieving speedups of 201× and 26×, respectively. The proposed approach has a potential to provide a powerful way to develop high accurate and efficient potentials even in the other systems.

DOI: 10.1103/PhysRevB.110.054110

I. INTRODUCTION

Interatomic potentials are widely used as the physical basis of molecular statics, molecular dynamics (MD), and Monte Carlo (MC) simulations in computational physics, chemistry, and materials science to predict or explain chemical reactions, physical processes, and material properties. Utilizing those traditional potentials, it is easy to carry out the simulations for large-scale systems exceeding ten million atoms and nanosecond timescales [1]. In such simulations, precisely predicting atomic and molecular forces and energies are crucial for both simulation stability and reliable results.

To date, there have been many functional forms of traditional potential, which are used to address different materials. For gas systems, the simple Lennard-Jones (LJ) potential [2] remains the popular choice, while metal systems often utilize more complex models like the embedded-atom method (EAM) [3,4], modified EAM (MEAM) [5], and angular-dependent potential (ADP) [6]. The MEAM and ADP contain angular components to consider the influence of bond angles between atoms in pure metals and alloys. These potentials are often recommended for use in conjunction with Ziegler-Biersak-Littmark [7] potential for radiation damage simulations. In addition, many-body potentials such as Tersoff [8], Stillinger-Weber [9], and other bond-order potentials [10] effectively capture the influence of many-body interactions in molecular systems and chemical reactions. For these many-body potentials, the functional forms are more complex than those of traditional pairwise potentials due to the complex structures of many-body parts [8].

Traditional potentials shine in terms of computational efficiency, particularly on modern parallel computing architectures like GPU and many-core processor devices. However, many studies demonstrated that the accuracy of those potentials is much less than the density-functional theory (DFT) calculations since only a small database obtained from DFT calculations or experiments was used for fitting the parameters of these potentials [1]. For instance, a widely used EAM potential [3] fails to predict the migration behavior of $1/2\langle 111\rangle$ screw dislocation, while another EAM potential struggles to capture $\langle 111\rangle$ mixed dislocation behavior [4,6]. Therefore, traditional potentials usually can only reproduce specific properties of materials. Accordingly, complex quantum-mechanically based bond-order potential (BOP) have been developed and proven to excel in predicting various material properties [11]. However, their computational cost remains a significant challenge, with BOP running approximately 633 times slower than traditional EAM potentials, as illustrated in Ref. [6].

Recently, machine-learning (ML) methods [6,12,13] driven by massive databases generated through DFT calculations, particularly those employing artificial neural networks (ANNs), are widely used to develop the highly accurate

*Contact author: meng_zhang@metall.t.u-tokyo.ac.jp

†Contact author: inoue@material.t.u-tokyo.ac.jp

interatomic potentials [14–16]. In ANN potentials, the descriptors, such as the Chebyshev polynomial [17] and the symmetry function developed by Behler [14], are used to describe the atomic environment, which are fed into the network to predict atomic energy and forces. During the training, a loss function based on atomic energy is extensively used to update network parameters [16,18]. As a result, ANN potentials have demonstrated the ability to achieve high accuracy in energy predictions, often within a few meV per atom compared to DFT results [1]. However, calculating forces remains computationally expensive due to the complex relationship between the atomic environment and the atomic energy inherently coming from the complexity of the neural network. This complexity limits the efficiency of the ML potential compared to the traditional potentials. Additionally, these potentials frequently suffer from low transferability [1], meaning their reliability of energy and force predictions for structures not included in the DFT database is uncertain.

To address the low transferability in ML potentials, physically informed neural network potentials (PINNs) have recently developed as a promising solution [1,19,20]. While PINN potential was also trained by a large DFT database, it uniquely integrates governing physics principles as a regularizing constraint. This distinctive approach improves the transferability, enabling them to effectively handle structures outside the training database [1,19]. Despite their advantages, PINN potentials continue to face a significant bottleneck in force calculation, exhibiting speeds approximately 100 times slower than traditional potentials [1].

Developing accurate and efficient interatomic potentials for molecular dynamics or Monte Carlo simulations remains a critical challenge. While recent advancements in machine learning have yielded promising frameworks such as neuroevolution potential [21], restricted multicanonical ensemble method [22], Green-Kubo method [23], Gaussian approximation potential [24,25], graph neural network [26], polynomial models [27], PINN [1,19], and others [28,29], their computational efficiency often hinders widespread adoption despite achieving first-principles accuracy. To overcome this limitation, continuous research is essential to develop novel, accurate, and high-performance potentials.

In this work, we proposed a ML potential framework, named artificial neural networks assistant (ANNA) potential, by combining ANN with physical models. Since the force calculation in ANNA potential is simplified, this potential shows quite higher performance in comparison with traditional ANN potential. Besides, the resulting ANNA potential, trained for body-centered cubic (bcc) iron, demonstrates high accuracy in property prediction. The proposed ANNA framework offers a promising approach to address this challenge by providing a pathway to develop high-accuracy and high-performance potentials for a wide range of systems.

II. METHODOLOGY

A. Angular-dependent potential

In the ANNA potential for BCC iron, an ADP potential [30] was selected as the physical basis which describes both pair- and bond-order effects, especially in distorted bonding environments around crystal defects [31]. The total energy E_{total} is given as

$$E_{\text{total}} = \sum_{i>j} \Phi(r_{ij}) + \sum_i F(\bar{\rho}_i) + \frac{1}{2}\sum_{i,\alpha}\left(\mu_i^{\alpha}\right)^2 + \frac{1}{2}\sum_{i,\alpha,\beta}\left(\lambda_i^{\alpha\beta}\right)^2 - \frac{1}{6}\sum_i v_i^2, \tag{1}$$

where i and j are the index of atoms. The first and second terms in Eq. (1) are the pair interaction between atoms and embedding energy, respectively, as those found in the conventional EAM model. To model these interactions, we employ a generalized LJ potential for the pair term and a simple polynomial function [4] for the embedding term, defined as follows:

$$\Phi(r_{ij}) = \psi\left(\frac{r_{ij}-r_c}{h}\right)\left[\frac{V_0}{b_2-b_1}\left(\frac{b_2}{z_1^{b_1}}-\frac{b_1}{z_1^{b_2}}\right)+\delta\right], \tag{2}$$

$$F(\bar{\rho}_i) = a_1\sqrt{\bar{\rho}_i} + a_2\bar{\rho}_i^2 \tag{3}$$

where r_c is the cutoff distance, set to be 5.055 Å based on the conventional ADP potential [30]. The z_1 in Eq. (2) is equal to r_{ij}/r_1, with r_{ij} being the distance between atoms i and j, and r_1 being a fitting parameter. The $\bar{\rho}_i$ is the host electron density at atom i caused by surrounding neighbor atoms (j), given as

$$\bar{\rho}_i = \sum_{j\ (j\neq i)} \psi\left(\frac{r_{ij}-r_c}{h}\right)[A_0 z_2^y e^{-\gamma z_2}(1+e^{-\gamma z_2})+C_0], \tag{4}$$

where $z_2 = r_{ij} - r_0$ and the first term in the summation is a cutoff function given as follows:

$$\psi(x) = \begin{cases} \frac{x^4}{1+x^4}, & \text{if } x < 0 \\ 0, & \text{otherwise} \end{cases}. \tag{5}$$

The angular contribution in Eq. (1) will be introduced by the noncentral components of bonding through vectors and given as

$$\mu_i^{\alpha} = \sum_{i\neq j} u(r_{ij}) r_{ij}^{\alpha}, \tag{6}$$

$$\lambda_i^{\alpha\beta} = \sum_{i\neq j} w(r_{ij}) r_{ij}^{\alpha} r_{ij}^{\beta}, \tag{7}$$

$$v_i = \sum_{\alpha} \lambda_i^{\alpha\alpha}, \tag{8}$$

where α and β refer to the Cartesian directions. $u(r_{ij})$ and $w(r_{ij})$ are the dipole and quadrupole functions, respectively, defined as

$$u(r_{ij}) = \psi\left(\frac{r_{ij}-r_c}{h}\right)(d_1 e^{-d_2 r_{ij}} + d_3), \tag{9}$$

$$w(r_{ij}) = \psi\left(\frac{r_{ij}-r_c}{h}\right)(q_1 e^{-q_2 r_{ij}} + q_3). \tag{10}$$

B. Training and implementation of the ANNA potential

Figure 1 illustrates the conceptual framework of the ANNA potential. Traditional interatomic potentials model the potential energy as a function of atomic coordinates with constant parameters shared by all atoms. PINN potentials, however, innovatively allow certain parameters to adapt based on the local atomic environment. This variation, the key idea behind

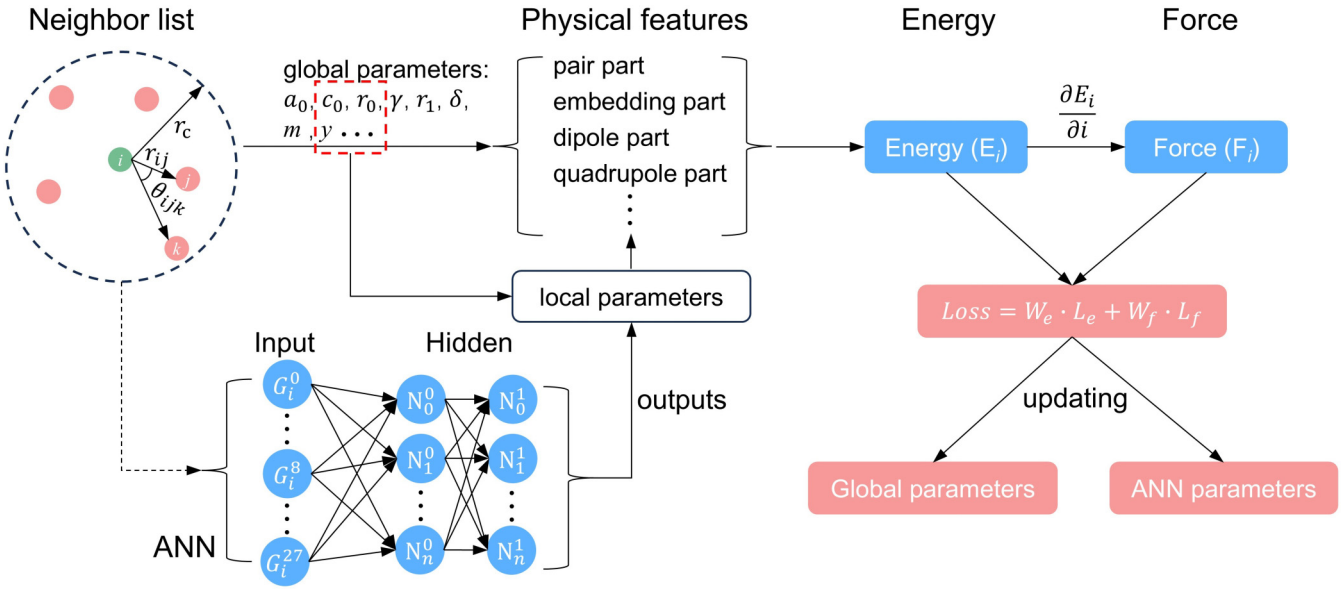

FIG. 1. Flowchart of the developed artificial neural networks assistant (ANNA) potential. As an input for the artificial neural network (ANN), 28 symmetry functions (G) including 9 radial and 19 angular contributions are selected. The parameters in the bottom-right corner are trained using the DFT database.

PINN approaches, involved estimating some or all parameters for each atomic coordinate using an ANN [1]. However, this approach necessitates calculating all the derivatives of the activation functions in each layer in ANN with respect to the atomic environment for force calculation, making it computationally expensive [32].

Our ANNA potential capitalizes on the assumption that a limited subset of subfunctions exhibits significant sensitivity to the atomic environment while remaining relatively stable for small atomic displacements within a specific range. We leverage this by strategically selecting these subfunctions, enabling us to safely neglect their derivatives in force calculations. Some parameters in these subfunctions are set to be "local parameters," which will be calculated through an ANN in order to account for the specific atomic environment, as shown in Fig. 1. Extensive trials revealed that the angular contributions in Eqs. (9) and (10) serve as the typical subfunctions, and d_2 and q_2 within these equations can be designated as the local parameters. This configuration provides consistently favorable training results. Supplemental Material, Fig. S1 [33] illustrates the variability of $u(r_{ij})$ and $w(r_{ij})$ for different atom pairs (i, j) when atom i is displaced by 0.25 Å, approximately 10% of the nearest-neighbor distance. The other 15 parameters in Eqs. (2)–(4) and (9) and (10) including V_0, b_2, b_1, r_1, r_0, h, δ, A_0, γ, y, C_0, d_1, q_1, d_3, and q_3 are treated as the "global parameters" throughout the training process.

The feedforward ANN architecture features a designed structure of 28 inputs, 2 hidden layers with 6 nodes each, and 2 outputs (d_2 and q_2). The modified hyperbolic tangent and linear functions were set as the activation functions in each hidden layer and output layer, respectively. Before training, only the atomic environment so called the "symmetry functions G" was calculated as the input, as shown in Fig. 1. The 9 radial and 19 angular G values were considered for the ANNA, which are the same as the ANN potential for bcc Fe [16]. The DFT database contained 6501 ferromagnetic (FM) structures was calculated by Mori and Ozaki and the detailed information is available in the Supplemental materials of Ref. [16]. Atomic structures in the database contain the point defects, surface, and unstable atomic structures with varying sizes, ranging from a few atoms to dozens. The global parameters in the physical model and the parameters including weights and biases in ANN were trained by adjusting these parameters to minimize the loss function, which consists of the errors of both energy and force, defined as follows:

$$\text{loss} = w_e \frac{1}{N_s} \sum_{i=0}^{N_s} (E_i - E_{\text{DFT}})^2 + w_f \frac{1}{3N_a} \sum_{\alpha=1}^{3} \sum_{j=0}^{N_a} \left(F_{j,\,\alpha} - F_{\text{DFT},\,\alpha}\right)^2, \quad (11)$$

where w_e and w_f are the weights for the errors of energy and force predictions compared to the DFT calculation, respectively. The N_s and N_a are the number of structures and atoms in the database, respectively. The $\alpha = 1, 2$, and 3 represent the Cartesian directions.

With the complete set of parameters for the bcc iron ANNA potential acquired, we implemented the potential in both central processing unit (CPU) and GPU versions within the LAMMPS [43] package guided by the flowchart in Fig. 1, and made it publicly accessible through GitHub [44].

III. COMPARISON OF POTENTIALS

Figure 2 shows the accuracy of the ANNA potential and the error distributions of atomic energy and force. The black dashed lines are the perfect-fitting line with a slope of 1.0. It can be found that the predicted energy and force are in excellent agreement with the values in the DFT database, which is better than the energy and force prediction by the

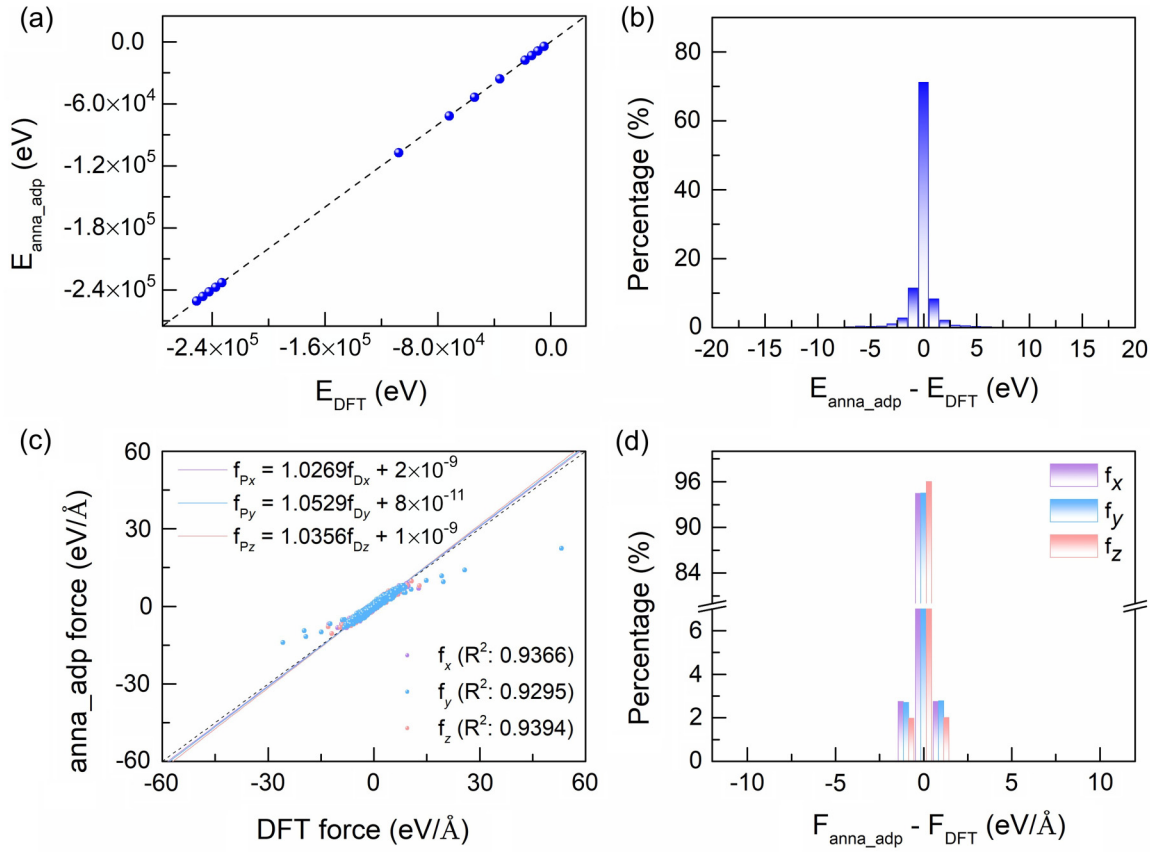

FIG. 2. Accuracy of the ANNA potential. (a) and (c), respectively, depict the comparison of energy and force predicted by anna_apd with respect to the reference DFT data, which contain more than 128 802 atoms; the dashed lines are the perfect fit with a slope equal to 1.0. (b) and (d) are the error distributions for the energy of structures and the force of atoms, respectively.

conventional ADP potential [6]. Quantitatively, the average error for energy prediction is about 0.063 eV per atom and the error for force predictions is approximately 0.1398 eV/Å per atom. Although the average force error per atom is small, the predictions from anna_adp for the atoms with large force deviate significantly from DFT forces. This trend is consistent with results from an ANN potential [16] and an eam_fs potential [3], particularly eam_fs, which exhibits the most significant overestimation. This behavior is attributed to two possible causes: (i) low force values predicted by Lennard-Jones–like analytical repulsion term; and (ii) only few atoms have large atomic forces within 128 802 atoms database. Therefore, expanding the database with more such structures is necessary to improve accuracy of anna_adp, which will be explored in future studies.

Variation models with different point defects, linear defects, and planar defects were constructed by using our developed code [45] or the ATOMSK [46] package to validate this potential. Detailed information about the crystalline structure of models and the parameters of simulation can be seen in Supplemental Material, Methods [33]. The structures including edge, mixed, screw dislocations, stacking faults, and grain boundaries for validation were also compared with the structures in DFT database to check the repeatability (similarity) between them. The results suggest these structures for validation differ substantially from those in the training database, as can be seen in Sec. C of the Supplemental Material [33].

Three established potentials, ANN potential (annp) [16], ADP potential (adp_new) [6], and EAM potential (eam_fs) [3], were adopted to demonstrate the prediction performance of the proposed ANNA potential. The training database of annp is the sub-database of this potential (anna_adp) and contains 5751 atomic structures [16].

A. Fundamental properties of bcc iron

Table I summarizes the fundamental properties of bcc iron predicted by four different potentials in comparison with the DFT calculation and experimental data. It can be found that most properties obtained by annp, adp_new, and anna_adp agree well with the DFT and experimental values, while the formation energies of monovacancy and divacancy, and surface energy predicted by eam_fs, show a large deviation from the reference data. The elastic constant of C_{12} predicted by adp_new is smaller than that of DFT results, while those predicted by annp and anna_adp are consistent with that by the DFT calculation [47]. In the simulation of interstitial formation energy, an additional atom will be randomly introduced into the matrix. Subsequently, energy minimization based on the potential allows the atom to find a stable position. However, the annp significantly overestimates the formation energy of an interstitial atom when the additional atom is randomly placed very close to the perfect matrix. The essential reason is that the additional atom will move to the perfect

TABLE I. Fundamental properties of bcc Fe predicted by four different potentials in comparison with experimental, first-principles, and tight-binding (TB) calculations. a_0 is equilibrium lattice parameter, C_{ij} is elastic constants, E_v^f is vacancy formation energy, E_{dv}^f are the divacancy formation energy at first-, second-, third-, fourth-, and fifth-nearest-neighbor distance, E_i^f is interstitial formation energy, and γ_s is surface energy.

Properties	Experiment	*Ab initio*/TB	annp	adp_new	eam_fs	anna_adp
a_0 (nm)	0.286 65[a]; 0.285 5[b]	0.2834[c]	0.283 56	0.282 96	0.285 5	0.283 74
C_{11} (GPa)	242[d]	297(288)[c]	274.68	250.39	243.36	294.58
C_{12} (GPa)	146.5[d]	151(148)[c]	176.90	108.04	145.01	162.11
C_{44} (GPa)	112[d]	105(102)[c]	110.27	110.07	116.04	107.79
E_v^f (eV)	2.0 ± 0.2[e]	1.93–2.02[f]; 2.07[g,h]	2.355	2.055	1.712	2.2613
E_{dv}^f (1NN) (eV)		4.265[i]; 4.24[j]	4.278	4.003	3.297	4.438
E_{dv}^f (2NN) (eV)		4.20[j]	4.001	3.919	3.188	4.262
E_{dv}^f (3NN) (eV)		4.45[j]	4.490	4.078	3.447	4.528
E_{dv}^f (4NN) (eV)			4.653	4.056	3.397	4.441
E_{dv}^f (5NN) (eV)			4.732	4.082	3.449	4.399
E_i^f [100] (eV)		4.37[f]; 4.64[g,h]	18.77(4.96)	4.572	4.195	4.446
E_i^f [110] (eV)		3.41[f]; 3.64[g,h]	17.66(3.94)	3.754	3.528	3.969
E_i^f [111] (eV)		4.11[f]; 4.34[g,h]	19.30(4.13)	4.352	4.01	3.694
γ_s (100) (J/m^2)	2.36[k]	2.543[j]; 2.29[l]	2.535	2.6045	1.785	2.30
γ_s (110) (J/m^2)	2.36[k]	2.495[j]; 2.27[l];	2.412	2.32	1.61	1.74
γ_s (111) (J/m^2)	2.36[k]	2.752[j]; 2.52[l]	2.626	2.688	1.971	2.489
γ_s (112) (J/m^2)		2.629[j]; 2.50[m]	2.613	2.578	1.857	2.20

[a]Reference [50].
[b]Reference [51].
[c]Without and with (values in parentheses) quasiharmonic zero-point energy contributions, Ref. [52].
[d]Reference [53].
[e]Reference [54].
[f]Reference [55].
[g]Reference [56].
[h]Reference [57].
[i]Reference [16].
[j]Reference [47].
[k]For average orientation, Ref. [60].
[l]Reference [58].
[m]Reference [59].

lattice site during energy minimization, which results in large system energy. This can be observed by comparing the values with those obtained by using the optimized structures (shown in parentheses within Table I).

Further evidence can be seen from the unusual behavior of the ground-state energy-volume curve of ferromagnetic (FM) iron calculated by spin dynamics MD [48,49] presented in Fig. 3. The result might have been induced by the fact that the database consists of the FM bcc structures with the lattice constant ranging only from 2.480 78 to 3.182 48 Å, which corresponds to the atomic volume ranging from 7.63 to 16.12 Å^3. Therefore, the generalizability of the annp is limited because its energy prediction deteriorates for the atomic volume without the database. Additionally, the annp shows a relatively large fluctuation when the atomic volume is small or large, as well as the eam_fs under the condition of large atomic volume. In the atomic volume range of 8 to 10 Å^3, both adp_new and eam_fs consistently underestimate the energy compared to the DFT values, as can be seen from the inset. However, these behaviors are not found from the curve predicted by anna_adp, which owes to a powerful synergy that the ANNA framework effectively integrates the physical foundation of atomic interactions with the exceptional adaptability and learning capabilities of neural networks.

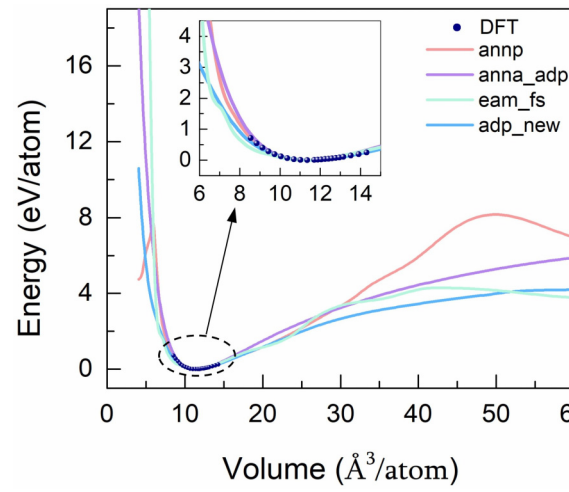

FIG. 3. Ground-state energy-volume for ferromagnetic (FM) bcc iron. The navy blue points indicate the DFT predictions [61].

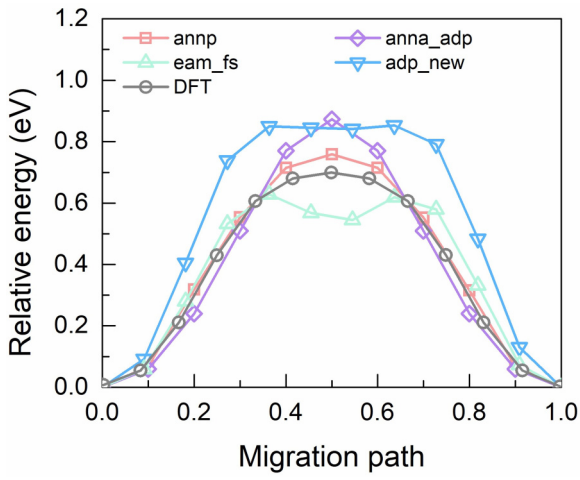

FIG. 4. Vacancy migration barrier at zero pressure and temperature predicted by four interatomic potentials. The gray points indicate the DFT calculations [6].

Since the DFT database was constructed assuming only FM state, the resulting anna_adp potential can primarily capture the properties of FM iron. The Curie temperature (T_c) was also estimated by using spin dynamics MD. The T_c value is about 900 K and close to the results obtained from adp_new potential and experiment (∼1045 K) [6,49]. To improve the accuracy of anna_adp for predicting the other magnetic states, the DFT database needs to be expanded by adding different magnetic states such as the antiferromagnetic, antiferromagnetic double layer, paramagnetic, and that with noncollinear spin directions. This will be a subject in future study. Therefore, the anna_adp potential is suitable for simulations under finite temperature, which is similar to the annp, adp_new, and eam_fs potentials.

B. Migration energy of monovacancy

The migration energy for monovacancy along the ⟨111⟩ direction can be seen in Fig. 4. Interestingly, the migration paths predicted by adp_new and eam_fs exhibit a double-hump profile, which is predominantly attributed to the presence of a metastable transition state, characterized by a localized minimum energy state along the migration path [6]. However, the results obtained from annp and anna_adp agree well with the DFT data, especially for the results from annp. The migration barriers for annp and anna_adp potentials are 0.7589 and 0.8727 eV, respectively. Based on these values, we further estimate the activation energy including the formation energy and migration barrier ($E_v^f + E_v^m$) of self-diffusion for monovacancy. The activation energy calculated by the adp_new is 2.908 eV, which is consistent with the experimental value 2.91 ± 0.04 eV [62,63]. The values for annp and anna_adp are 3.114 and 3.134 eV, respectively, and slightly larger than the experimental value. The eam_fs potential predicts a small activation energy (2.34 eV) due to the small E_v^f and E_v^m.

C. Dislocation behavior

Accurately capturing dislocation activities and their core structures is crucial for predicting the behavior of metals during deformation processes. In this work, two typical dislocations in bcc iron, the screw dislocation (S111) and the 70.5° mixed dislocation (M111), are considered to investigate the migration behavior. These two dislocations have the same Burgers vector $b = \frac{a_0}{2}\langle 111\rangle$ with a_0 being lattice parameter, as visualized in Supplemental Material, Fig. S3 [33]. The S111 has a compact, nonplanar core, which results in a comparably large Peierls stress and non-Schmid behavior [64,65]. Unlike S111, the M111 shows the planar core and is expected to have low Peierls stress [6,65]. Based on DFT results [47,66], it is known that the core structure of S111 can be divided into three types, i.e., the nondegenerate ground-state so-called "easy" core (E), the split core (S), and the hard core (H).

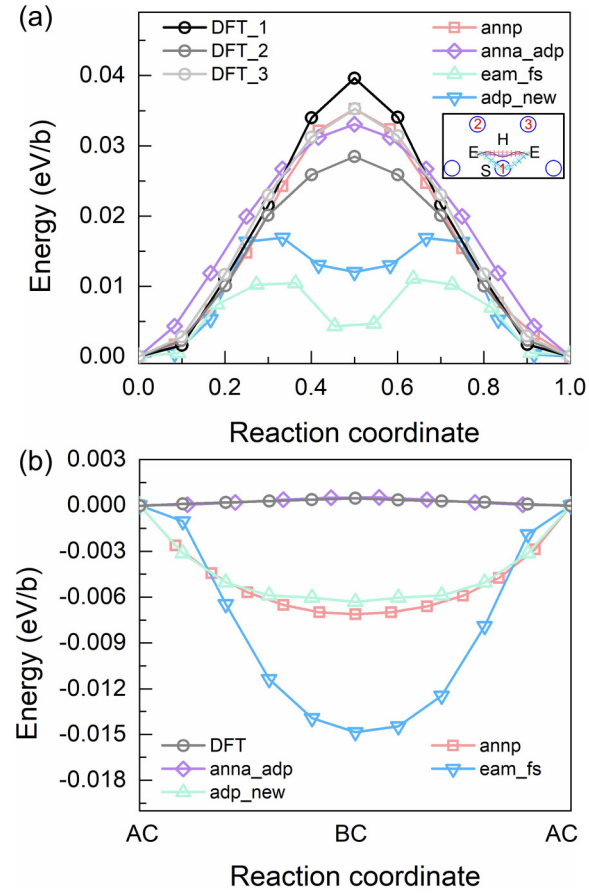

FIG. 5. Nudged elastic band (NEB) calculations for (a) $a_0/2\langle 111\rangle$ screw dislocation and (b) $a_0/2\langle 111\rangle$ 70.5° mixed dislocation. The inset in (a) displays the dislocation trajectories predicted by the four potentials and the DFT results distinguished by the method of cost function (red line) and disregistry (black line) [68]. DFT_1 and DFT_2 values in (a) are obtained from Ref. [67] and DFT_3 values are from Ref. [68]. The gray points in (b) are the DFT calculations [6].

Figure 5(a) shows the variation of Peierls potential with the transition path for S111 from easy to easy cores. The inset displays the dislocation core locations for the four potentials and DFT results (detailed calculations in Supplemental Material, Eqs. (1) and (2) [33]). Notably, the adp_new and eam_fs potentials exhibit a marked inadequacy in capturing the true behavior of the dislocation. The double-hump profiles suggest

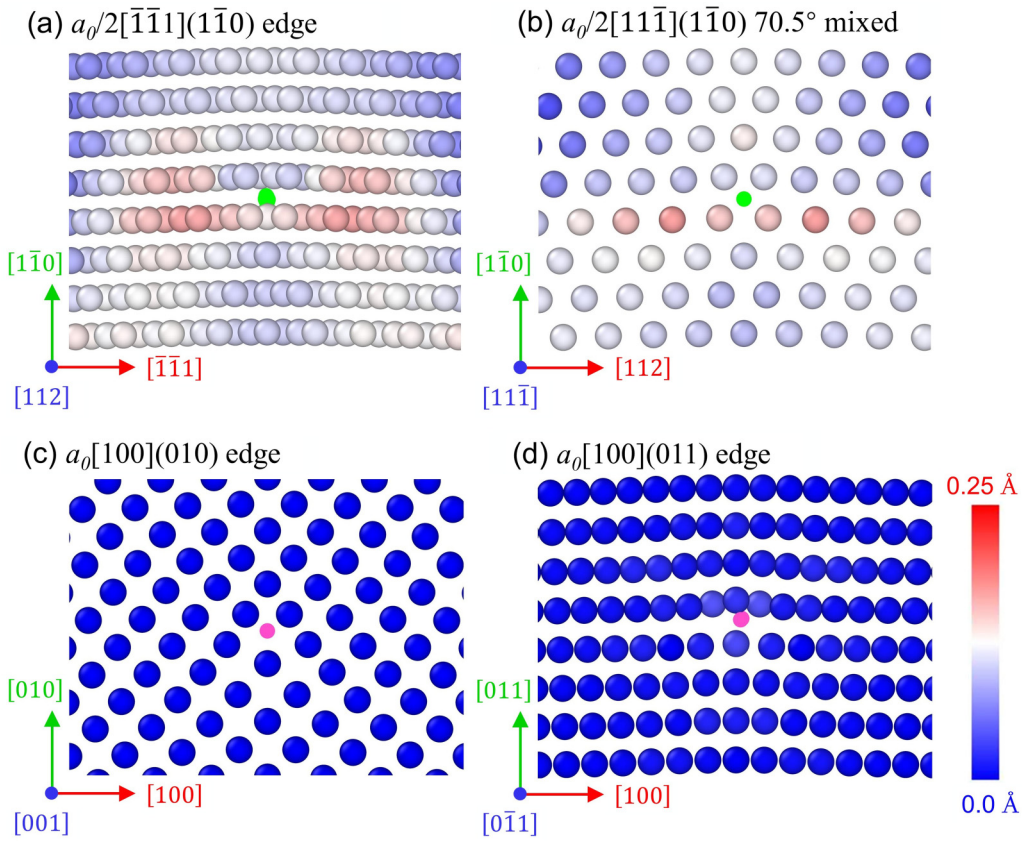

FIG. 6. Atomic configuration of dislocation cores for (a) $a_0/2\langle 111\rangle\{110\}$ edge, (b) BC core of a $a_0/2\langle 111\rangle\{110\}$ 70.5° mixed, (c) $a_0\langle 100\rangle\{100\}$ edge, and (d) $a_0\langle 100\rangle\{110\}$ edge dislocations. The atomic color shows the error norm from DFT results [70]. The green and magenta lines are the dislocation lines perpendicular to the screen.

the presence of a local minimum intermediate state [6]. The fundamental reason for the deficiency lies in the fact that the migration paths predicted by the two potentials are close to split core, deviating from the actual transition path. The results obtained from the annp and anna_adp potentials show a single-hump profile and the barriers are 0.035 26 and 0.033 08 eV, respectively, which are in good agreement with the DFT value (0.028 48–0.0396 eV) [67,68] and the experimental result (0.037 eV) [69]. In addition, the migration path predicted by the anna_adp is slightly concave, which is mostly close to the DFT-calculated path compared with the curve obtained from annp.

For $M111$, the changing of dislocation center along the $\langle 112\rangle$ direction on the $\{110\}$ glide plane results in two distinct core configurations: (i) AC core, where the core centers on atoms; and (ii) BC core, where the core lies on the center of bonds between atoms [65]. Based on the DFT calculations and BOP potential analysis, we know that the AC core in bcc iron corresponds to the ground state with minimum energy and the BC core represents the transition state [6,65]. In addition, the DFT results in Fig. 5(b) show an extremely small energy difference between AC and BC core configurations [6,65]. Only the anna_adp predicts both the same variation in transition energy as the DFT curve and a closely matching Peierls barrier (0.000 519 eV for anna_adp and 0.000 4727 eV for DFT). In contrast, the other potentials predict large barriers and a reversed stability of the cores, especially for the eam_fs potential. The relaxed simulation, detailed in Supplemental Material, Fig. S4 [33], further demonstrates that only the anna_adp predicts the AC cores as the minimum energy configuration. The animation of the dislocation moving from AC to AC cores for all four potentials can be seen in the Supplemental Material, Movies 1–4.

To further evaluate the anna_adp potential's accuracy for dislocation modeling in bcc iron, we calculated core structures of different dislocations including $a_0/2\langle 111\rangle\{110\}$ edge, $M111$, $a_0\langle 100\rangle\{100\}$ edge, and $a_0\langle 100\rangle\{110\}$ edge dislocations, and compared them with corresponding DFT calculations [70]. Figure 6 shows the atomic configuration and the colors are the error normal [16] ($\sqrt{|\boldsymbol{r}_i^{\text{potential}} - \boldsymbol{r}_i^{\text{DFT}}|}$) of the atomic positions ($\boldsymbol{r}_i$) between the results predicted by anna_adp and DFT calculations. The error norms for $a_0\langle 100\rangle\{100\}$, and $a_0\langle 100\rangle\{110\}$ edge dislocations are remarkably small, indicating the exceptional consistency between the core configurations calculated by the potential and those obtained from DFT calculations. Although error norms of the $a_0/2\langle 111\rangle\{110\}$ edge and the $M111$ dislocation cores are slightly larger than those of the other two edge dislocations, the maximum error norm of these cores is still less than 0.17 Å. Therefore, these results demonstrate that the ANNA potential can accurately capture the core structure of dislocations.

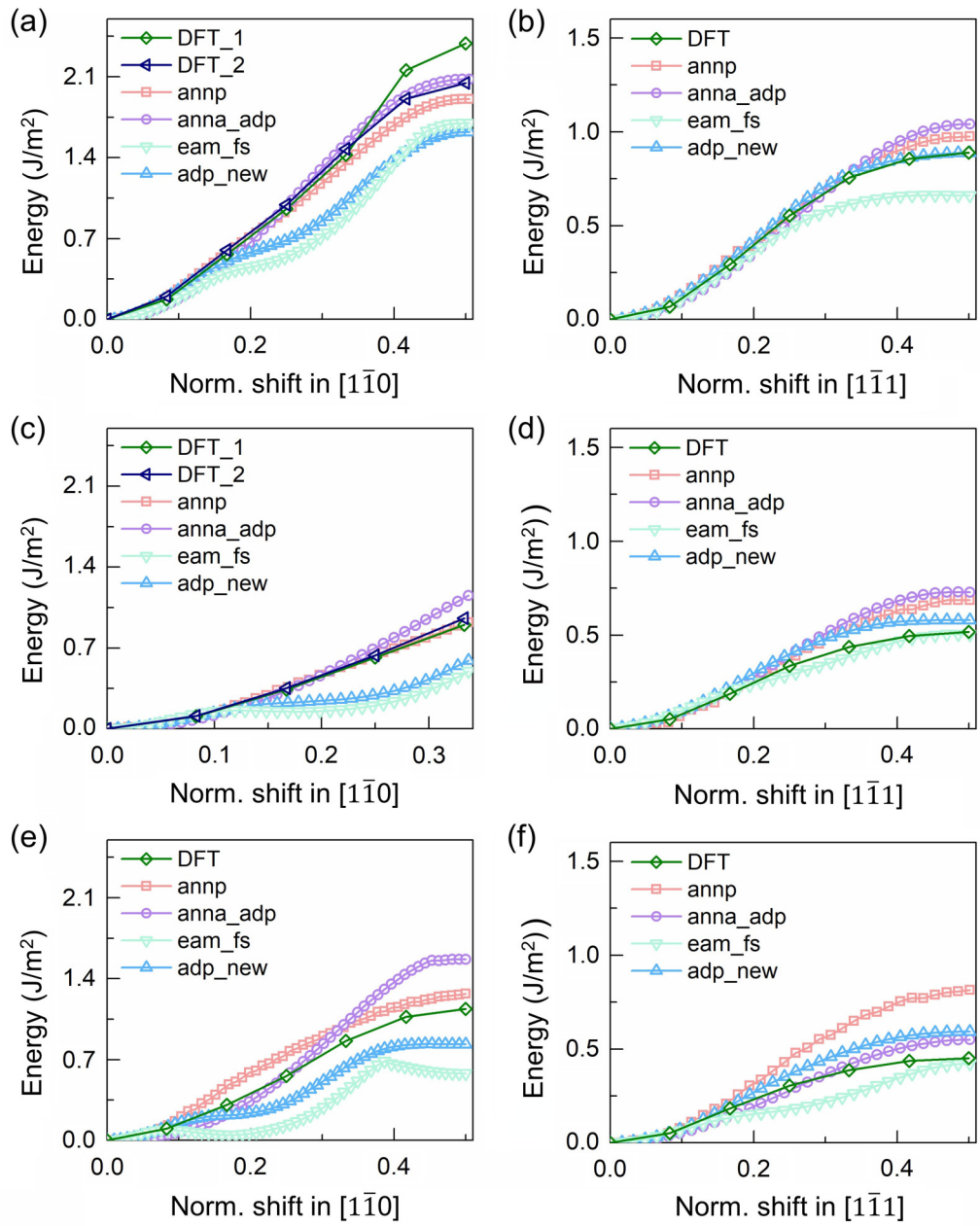

FIG. 7. Generalized stacking-fault energy (GSFE) curves of the (110) glide plane in [1$\bar{1}$0] and [1$\bar{1}$1] directions as a function of external loads: (a), (b) no external load; (c), (d) 7.5% uniaxial strain; (e), (f) 5.0% equibiaxial strain. The olive and navy blue points are the DFT calculations [71].

D. Generalized stacking-fault energy

It has been known long time that the stable stacking fault generated by dislocation dissociation in the bcc metals is not possible. However, when the area has an extremely large stress compared to the stress-free area, this phenomenon could also be observed in bcc metals [71]. The experimental results for bcc iron show the dislocation dissociation on {110} plane [72]. Additionally, atomic simulations have revealed the formation of stacking fault in bcc models under highly strained systems, e.g., crack tips [73] and nanobeams subjected to tension [74] and bending [75].

Therefore, we created two models to investigate the generalized stacking-fault energy (GSFE) under the following conditions: no external load, 7.5% uniaxial strain, and 5.0% equibiaxial strain (Supplemental Material, Methods [33]). Figure 7 shows the results predicted by all four potentials in comparison with DFT calculations. A notable feature of eam_fs and adp_new is that their GSFE curves differ significantly from the shape of DFT results in most cases. Both potentials exhibit remarkable changes in the curvature of their GSFE curves, shifting from positive to negative and back again, forming a shoulderlike shape when the normalized shift is larger than 0.05 in [1$\bar{1}$0] directions [71]. Similarly, the curve predicted by eam_fs potential in [1$\bar{1}$1] direction under equibiaxial strain also shows a shoulderlike feature, which corresponds to the unphysical structures with the formation

of local minimum [16,71]. However, this phenomenon is not observed for anna_adp and annp potentials. The most GSFE curves predicted by the two potentials are close to the DFT calculations. The GSFE curve of (112) glide plane in [1$\bar{1}$1] direction, with no external load, for the four potentials can be seen in Supplemental Material, Fig. S5 [33]. All curves exhibit the same shape as DFT results, but the value predicted by eam_fs for the normalized shift larger than 0.25 is lower than those of others.

E. Grain-boundary energy

Grain boundaries not only govern the mechanical properties of nanocrystalline [76,77] or martensite steel with complex hierarchical boundaries [78] but also provide the energetically favorable positions for the source or sink of point defects [79] or dislocation [80]. Two types of dislocations, the symmetry-tilt grain boundary (STGB) and twist grain boundary (TWGB), were considered for validation purposes. The detailed structure of the two types of boundaries can be seen in Supplemental Material, Tables S1 and S2 [33].

The energies for the 46 STGBs with misorientation angle (θ_m) ranging from 11.6° to 168.5° [81] and the 21 TWGBs with θ_m ranging from 1.59° to 86.63° [82] are shown in Fig. 8. For both types of GBs, the energies predicted by the adp_new and eam_fs are generally lower than those obtained by the other two potentials and DFT calculations. This trend is particularly noticeable for STGB energies calculated by eam_fs and TWGB energies predicted by adp_new. The STGB energies predicted by the eam_fs and anna_adp significantly differ from those of DFT by approximately 18.66 and 14.07% on average, respectively. However, annp and anna_adp in most cases demonstrate the ability to capture accurate results for two types of GBs. This is potentially attributed to their training database that consists of point defects, surface, and unstable atomic structures [81]. The STGB energies calculated using these two potentials exhibit minor deviations from DFT calculations, with 4.58% for annp and 7.11% for anna_adp on average. Although the annp shows close agreement with the reference data, it occasionally predicts less accurate results when the GB structure contains the atomic pair with a short distance. This phenomenon can be seen from the energy for $\theta_m = 2.7°$ TWGB in Fig. 8(b), which might be attributed to the strange behavior of ground-state energy-volume curve at small range of atomic volume, as shown in Fig. 3.

F. Phonon density of states

Phonons, associated with the lattice vibrations in crystalline materials, reflect many physical properties of materials such as thermal conductivity [84], heat capacity [85], sound velocity, and elastic constants in solid [86]. Here, the phonon density of states (DOS) was calculated by using the four potentials, as shown in Fig. 9. The results obtained from most potentials are in good agreement with the experimental data (black dashed line) [87], especially for the high-frequency region. Only the eam_fs potential exhibits a slight deviation from the reference data.

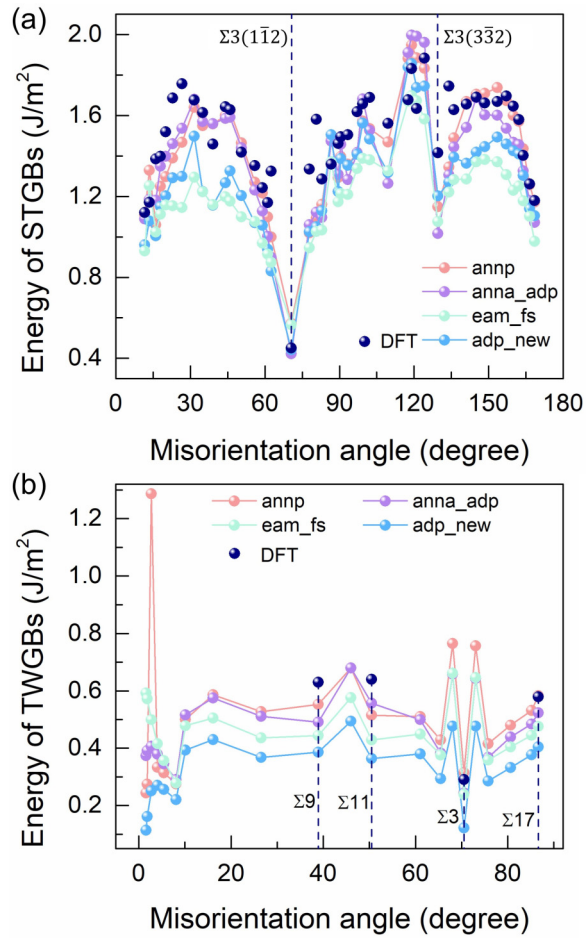

FIG. 8. Grain-boundary energies for (a) symmetric tilt grain boundaries (STGBs) and (b) twist grain boundaries (TWGBs). The navy blue points in (a) and (b) are the results of the DFT calculation from Ref. [81] and Ref. [83], respectively.

G. Computational performance

Figure 10 shows the computational performance of the GPU-implemented anna_adp compared with both 12-MPI

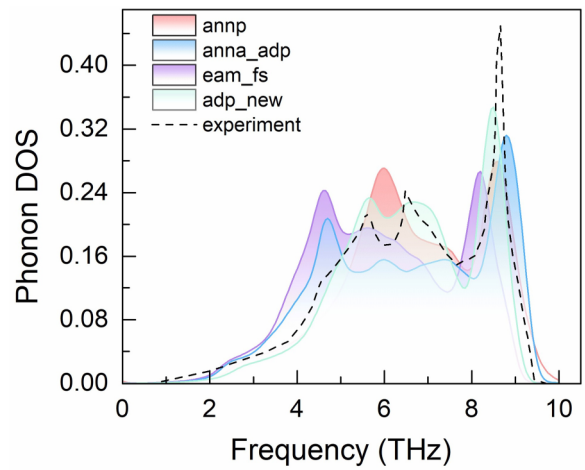

FIG. 9. Phonon DOS for bcc Fe calculated by using the four interatomic potentials. The black dashed line is experimental data [87].

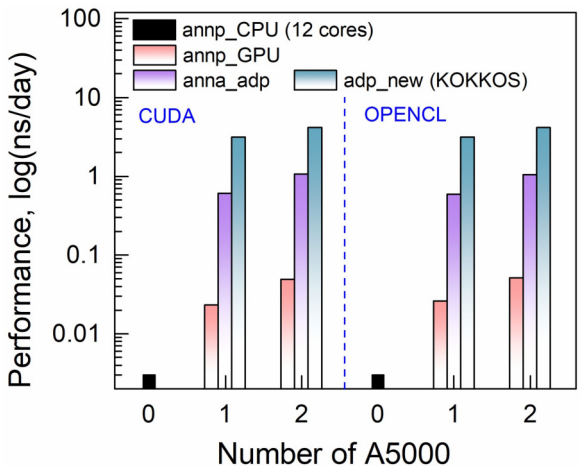

FIG. 10. Computational performance using a large model (152 880 atoms) after running 1000 time steps compared with: 12-MPI (message passing interface) tasks CPU-only of annp [16], GPU-accelerated annp [32], and adp_new potential accelerated by KOKKOS Library. For the case of two GPU cards, 2-MPI tasks were used.

tasks CPU-only runs of annp, GPU-accelerated annp [32], and GPU-accelerated adp_new by KOKKOS Library [88]. All the values were obtained using the neighbor list generated by CPU device and stored in random access memory. For the GPU runs, the list is transferred to the GPU device upon updating, which introduces a minor time overhead. Detailed benchmark information can be seen in Supplemental Material, Methods [33]. It can be found that anna_adp shows remarkable performance on a single GPU card, achieving 0.605 ns per day for compute unified device architecture (CUDA)- and 0.592 ns per day for open computing language (OPENCL) builds. The performances are 201 and 197 times faster than the 12-MPI tasks CPU-only runs of annp (0.003 ns per day), which is essentially attributed to simplified force calculation methodology. Furthermore, utilizing two GPU cards yields an approximate doubling of performance relative to a single card. Impressively, anna_adp also surpasses the GPU-accelerated annp by achieving a speedup of about 26× and 22× for CUDA- and OPENCL builds by using a single GPU card, respectively. This substantial performance enhancement enables simulations spanning larger temporal and spatial scales. When the neighbor list builds on a GPU device, anna_adp performance exhibits a slight further improvement for CUDA- and OPENCL builds.

Compared with traditional adp_new potential accelerated by KOKKOS Library [88], the performance of anna_adp (0.605 ns per day) is approximately 5.1 times slower than that of adp_new (3.116 ns per day), which is caused by the artificial neural network term in anna_adp. Although the physical models for both potentials are the same, the computational cost of 28 symmetry functions and forward propagation of ANN per atom in anna_adp is also high. The performance difference between the two potentials for two GPU cards becomes small (4.02 ns per day for adp_new, 1.062 ns per day, and 1.045 ns per day for anna_adp CUDA- and OPENCL builds, respectively). The reason is that KOKKOS Library always uses the undesirable thread-safe atomic operation for updating the forces of neighbors [89,90], which has a limitation on the performance. The limitation will become serious for the multiple CPU cores running because of the interprocess communication for the ghost atoms (atoms copied from the neighboring domain).

Additionally, the anna_adp shows lower performance compared with eam_fs potential accelerated by using KOKKOS Library (about 10.4 and 8.9 times slower by using a single and two GPU cards with CUDA build, respectively). Two additional terms of angular and ANN in anna_adp are the essential reason for the low performance of the potential compared with eam_fs, but these two terms significantly increase the accuracy of the anna_adp potential. Another important reason for the high performance of adp_new and eam_fs is that the embedding function, electron density function, and pair-interaction function are provided in a tabulated format by interpolation approach and the values are stored in the memory [43,91]. Therefore, these energy function values for different atomic pairs can be searched from the energy tables, which are very efficient. Hence, the implementation of eam terms in anna_adp will be modified in the next step to support the energy tables, which may further improve the performance of anna_adp.

IV. CONCLUSIONS

In summary, an approach has been developed to train the ANNA potential by incorporating a neural network into typical physical functions that exhibit insensitivity to atomic displacements within a specific range. The resulting ANNA potential for bcc iron demonstrates superior accuracy in predicting a wide range of iron properties, including point defects, dislocations, surfaces, stacking faults, and grain boundaries.

Crucially, this approach effectively addresses a major limitation of traditional machine-learning potential and PINN potentials, namely, their relatively low performance. It can also be used to develop ANNA potentials for other binary or multielement alloys to achieve the highly accurate and efficient MD simulations. However, identifying the above-mentioned optimal physical functions for training a given potential remains a challenge. For alloy system, the input (symmetry functions, G) of ANN might be different from the pure metal since different element pairs require different parameters of G. Therefore, the Behler-Parrinello symmetry functions might be a better choice for alloy [14,15]. Collaborative efforts are underway to develop a platform for training this ANNA potential, and the results will be reported in a forthcoming publication.

ACKNOWLEDGMENTS

We are grateful to Dr. Mori for providing the DFT database of iron and PYTHON code for analyzing some results. The implementations of the CPU and GPU versions of the ANNA potential are available in our GitHub repository or by contacting the authors directly. This work was supported by the Council for Science, Technology and Innovation (CSTI), Cross-ministerial Strategic Innovation Promotion Program

(SIP), "Materials Integration" for Revolutionary Design System of Structural Materials (Funding agency: JST), and Japan Society for the Promotion of Science (JSPS) KAKENHI Grant No. 22H01840. This work was also supported by the Ministry of Education, Culture, Sports, Science and Technology (MEXT) Program: Data Creation and Utilization-Type Material Research and Development Project Grant No. JPMXP1122684766.

[1] G. P. P. Pun, R. Batra, R. Ramprasad, and Y. Mishin, Physically informed artificial neural networks for atomistic modeling of materials, Nat. Commun. **10**, 2339 (2019).

[2] T. X. Nguyen, S. K. Bhatia, and D. Nicholson, Prediction of high-pressure adsorption equilibrium of supercritical gases using density functional theory, Langmuir **21**, 3187 (2005).

[3] M. I. Mendelev, S. Han, D. J. Srolovitz, G. J. Ackland, D. Y. Sun, and M. Asta, Development of new interatomic potentials appropriate for crystalline and liquid iron, Philos. Mag. **83**, 3977 (2003).

[4] L. Proville, D. Rodney, and M. C. Marinica, Quantum effect on thermally activated glide of dislocations, Nat. Mater. **11**, 845 (2012).

[5] S. A. Etesami and E. Asadi, Molecular dynamics for near melting temperatures simulations of metals using modified embedded-atom method, J. Phys. Chem. Solids **112**, 61 (2018).

[6] S. Starikov, D. Smirnova, T. Pradhan, Y. Lysogorskiy, H. Chapman, M. Mrovec, and R. Drautz, Angular-dependent interatomic potential for large-scale atomistic simulation of iron: Development and comprehensive comparison with existing interatomic models, Phys. Rev. Mater. **5**, 063607 (2021).

[7] J. F. Ziegler, M. D. Ziegler, and J. P. Biersack, SRIM - The stopping and range of ions in matter, Nucl. Instrum. Methods Phys. Res., Sect. B, **268**, 1818 (2010).

[8] T. D. Nguyen, GPU-accelerated Tersoff potentials for massively parallel Molecular Dynamics simulations, Comput. Phys. Commun. **212**, 113 (2017).

[9] W. M. Brown and M. Yamada, Implementing molecular dynamics on hybrid high performance computers-Three-body potentials, Comput. Phys. Commun. **184**, 2785 (2013).

[10] B. A. Gillespie, X. W. Zhou, D. A. Murdick, H. N. G. Wadley, R. Drautz, and D. G. Pettifor, Bond-order potential for silicon, Phys. Rev. B **75**, 155207 (2007).

[11] M. Mrovec, D. Nguyen-Manh, C. Elsässer, and P. Gumbsch, Magnetic bond-order potential for iron, Phys. Rev. Lett. **106**, 246402 (2011).

[12] F. Maresca, D. Dragoni, G. Csányi, N. Marzari, and W. A. Curtin, Screw dislocation structure and mobility in body centered cubic Fe predicted by a Gaussian approximation potential, npj Comput. Mater. **4**, 69 (2018).

[13] S. Chmiela, H. E. Sauceda, K. R. Müller, and A. Tkatchenko, Towards exact molecular dynamics simulations with machine-learned force fields, Nat. Commun. **9**, 3887 (2018).

[14] J. Behler and M. Parrinello, Generalized neural-network representation of high-dimensional potential-energy surfaces, Phys. Rev. Lett. **98**, 146401 (2007).

[15] J. Behler, R. Martonak, D. Donadio, and M. Parrinello, Pressure-induced phase transitions in silicon studied by neural network-based metadynamics simulations, Phys. Status Solidi B **245**, 2618 (2008).

[16] H. Mori and T. Ozaki, Neural network atomic potential to investigate the dislocation dynamics in bcc iron, Phys. Rev. Mater. **4**, 040601(R) (2020).

[17] N. Artrith, A. Urban, and G. Ceder, Efficient and accurate machine-learning interpolation of atomic energies in compositions with many species, Phys. Rev. B **96**, 014112 (2017).

[18] N. Artrith and A. Urban, An implementation of artificial neural-network potentials for atomistic materials simulations: Performance for TiO, Comput. Mater. Sci. **114**, 135 (2016).

[19] G. P. P. Pun, V. Yamakov, J. Hickman, E. H. Glaessgen, and Y. Mishin, Development of a general-purpose machine-learning interatomic potential for aluminum by the physically informed neural network method, Phys. Rev. Mater. **4**, 113807 (2020).

[20] Y. S. Lin, G. P. P. Pun, and Y. Mishin, Development of a physically-informed neural network interatomic potential for tantalum, Comput. Mater. Sci. **205**, 111180 (2022).

[21] Z. Y. Fan, Z. Z. Zeng, C. Z. Zhang, Y. Z. Wang, K. K. Song, H. K. Dong, Y. Chen, and T. A. Nissila, Neuroevolution machine learning potentials: Combining high accuracy and low cost in atomistic simulations and application to heat transport, Phys. Rev. B **104**, 104309 (2021).

[22] K. Miwa, Restricted multicanonical sampling for machine learning potential construction, Phys. Rev. B **107**, 054313 (2023).

[23] M. F. Langer, F. Knoop, C. Carbogno, M. Scheffler, and M. Rupp, Heat flux for semilocal machine-learning potentials, Phys. Rev. B **108**, L100302 (2023).

[24] P. Rowe, G. Csányi, D. Alfè, and A. Michaelides, Development of a machine learning potential for graphene, Phys. Rev. B **97**, 054303 (2018).

[25] J. Byggmästar, A. Hamedani, K. Nordlund, and F. Djurabekova, Machine-learning interatomic potential for radiation damage and defects in tungsten, Phys. Rev. B **100**, 144105 (2019).

[26] H. Y. Yu, Y. Zhong, L. L. Hong, C. S. Xu, W. Ren, X. A. Gong, and H. J. Xiang, Spin-dependent graph neural network potential for magnetic materials, Phys. Rev. B **109**, 144426 (2024).

[27] A. Seko, Machine learning potentials for multicomponent systems: The Ti-Al binary system, Phys. Rev. B **102**, 174104 (2020).

[28] C. Zeni, A. Anelli, A. Glielmo, and K. Rossi, Exploring the robust extrapolation of high-dimensional machine learning potentials, Phys. Rev. B **105**, 165141 (2022).

[29] E. T. Dubois, J. Tranchida, J. Bouchet, and J. B. Maillet, Atomistic simulations of nuclear fuel UO2 with machine learning interatomic potentials, Phys. Rev. Mater. **8**, 025402 (2024).

[30] Y. Mishin, M. J. Mehl, and D. A. Papaconstantopoulos, Phase stability in the Fe-Ni system: Investigation by first-principles calculations and atomistic simulations, Acta Mater. **53**, 4029 (2005).

[31] D. E. Smirnova, A. Y. Kuksin, and S. V. Starikov, Investigation of point defects diffusion in bcc uranium and U-Mo alloys, J. Nucl. Mater. **458**, 304 (2015).

[32] M. Zhang, K. Hibi, and J. Inoue, GPU-accelerated artificial neural network potential for molecular dynamics simulation, Comput. Phys. Commun. **285**, 108655 (2023).

[33] See Supplemental Material at http://link.aps.org/supplemental/10.1103/PhysRevB.110.054110 for the variation of two functions in adp potential with changing atomic positions; the similarity between structures for validation and training dataset; the detailed information of simulation methods and models; the results of relaxing simulation for 70.5° mixed dislocation; the results of generalized stacking-fault energy (GSFE) curves of the (112) glide plane in $[1\bar{1}1]$ direction; and which includes Refs. [34–42].

[34] A. Stukowski, Visualization and analysis of atomistic simulation data with OVITO-the Open Visualization Tool, Model. Simul. Mater. Sci. **18**, 015012 (2010).

[35] A. Stukowski and K. Albe, Dislocation detection algorithm for atomistic simulations, Model. Simul. Mater. Sci. **18**, 025016 (2010).

[36] L. T. Kong, G. Bartels, C. Campañá, C. Denniston, and M. H. Müser, Implementation of Green's function molecular dynamics: An extension to LAMMPS, Comput. Phys. Commun. **180**, 1004 (2009).

[37] https://github.com/atomisticnet/aenet.

[38] G. Henkelman and H. Jónsson, Improved tangent estimate in the nudged elastic band method for finding minimum energy paths and saddle points, J. Chem. Phys. **113**, 9978 (2000).

[39] M. Itakura, H. Kaburaki, and M. Yamaguchi, First-principles study on the mobility of screw dislocations in bcc iron, Acta Mater. **60**, 3698 (2012).

[40] Y. Wang, J. B. Liu, J. H. Li, J. N. Mei, Z. C. Li, W. S. Lai, and F. Xue, Machine-learning interatomic potential for radiation damage effects in bcc-iron, Comput. Mater. Sci. **202**, 110960 (2022).

[41] Z. H. Liu, Y. X. Feng, and J. X. Shang, Characterizing twist grain boundaries in BCC Nb by molecular simulation: Structure and shear deformation, Appl. Surf. Sci. **370**, 19 (2016).

[42] L. Ventelon and F. Willaime, Generalized stacking-faults and screw-dislocation core-structure in bcc iron: A comparison between ab initio calculations and empirical potentials, Philos. Mag. **90**, 1063 (2010).

[43] S. Plimpton, Fast parallel algorithms for short-range molecular-dynamics, J. Comput. Phys. **117**, 1 (1995).

[44] https://github.com/inouejunyalab/Meng_Zhang/tree/main/anna-gpu-lammps.

[45] https://github.com/inouejunyalab/Meng_Zhang/tree/main.

[46] P. Hirel, Atomsk: A tool for manipulating and converting atomic data files, Comput. Phys. Commun. **197**, 212 (2015).

[47] D. Dragoni, T. D. Daff, G. Csányi, and N. Marzari, Achieving DFT accuracy with a machine-learning interatomic potential: Thermomechanics and defects in bcc ferromagnetic iron, Phys. Rev. Mater. **2**, 013808 (2018).

[48] J. Tranchida, S. J. Plimpton, P. Thibaudeau, and A. P. Thompson, Massively parallel symplectic algorithm for coupled magnetic spin dynamics and molecular dynamics, J. Comput. Phys. **372**, 406 (2018).

[49] S. Nikolov, M. A. Wood, A. Cangi, J. B. Maillet, M. C. Marinica, A. P. Thompson, M. P. Desjarlais, and J. Tranchida, Data-driven magneto-elastic predictions with scalable classical spin-lattice dynamics, npj Comput. Mater. **7**, 153 (2021).

[50] C. Kittel, *Introduction to Solid State Physics* (John Wiley & Sons, New York, 2005).

[51] Z. S. Basinski, W. Humerothery, and A. L. Sutton, The lattice expansion of iron, Proc. R. Soc London, Ser. A **229**, 459 (1955).

[52] D. Dragoni, D. Ceresoli, and N. Marzari, Thermoelastic properties of α-iron from first-principles, Phys. Rev. B **91**, 104105 (2015).

[53] J. P. Hirth, J. Lothe, and T. Mura, *Theory of Dislocations*, 2nd ed. (John Wiley & Sons, New York, 1983).

[54] L. D. Schepper, D. Segers, L. Dorikensvanpraet, M. Dorikens, G. Knuyt, L. M. Stals, and P. Moser, Positron-annihilation on pure and carbon-doped alpha-iron in thermal-equilibrium, Phys. Rev. B **27**, 5257 (1983).

[55] C. Domain and C. S. Becquart, Ab initio calculations of defects in Fe and dilute Fe-Cu alloys, Phys. Rev. B **65**, 024103 (2001).

[56] C. C. Fu, F. Willaime, and P. Ordejón, Stability and mobility of mono- and di-interstitials in α-Fe, Phys. Rev. Lett. **92**, 175503 (2004).

[57] C. C. Fu, J. Dalla Torre, F. Willaime, J. L. Bocquet, and A. Barbu, Multiscale modelling of defect kinetics in irradiated iron, Nat. Mater. **4**, 68 (2005).

[58] M. J. S. Spencer, A. Hung, I. K. Snook, and I. Yarovsky, Density functional theory study of the relaxation and energy of iron surfaces, Surf. Sci. **513**, 389 (2002).

[59] P. Błoński and A. Kiejna, Structural, electronic, and magnetic properties of bcc iron surfaces, Surf. Sci. **601**, 123 (2007).

[60] W. R. Tyson and W. A. Miller, Surface free-energies of solid metals - estimation from liquid surface-tension measurements, Surf. Sci. **62**, 267 (1977).

[61] K. Wang, S. L. Shang, Y. Wang, Z. K. Liu, and F. Liu, Martensitic transition in Fe via Bain path at finite temperatures: A comprehensive first-principles study, Acta Mater. **147**, 261 (2018).

[62] M. Lübbehusen and H. Mehrer, Self-diffusion in α-iron: The influence of dislocations and the effect of the magnetic phase transition, Acta Metall. Mater. **38**, 283 (1990).

[63] A. Seeger, Lattice vacancies in high-purity α-iron, Phys. Status Solidi A **167**, 289 (1998).

[64] A. Kraych, E. Clouet, L. Dezerald, L. Ventelon, F. Willaime, and D. Rodney, Non-glide effects and dislocation core fields in BCC metals, npj Comput. Mater. **5**, 109 (2019).

[65] L. Romaner, T. Pradhan, A. Kholtobina, R. Drautz, and M. Mrovec, Theoretical investigation of the 70.5° mixed dislocations in body-centered cubic transition metals, Acta Mater. **217**, 117154 (2021).

[66] C. Domain and G. Monnet, Simulation of screw dislocation motion in iron by molecular dynamics simulations, Phys. Rev. Lett. **95**, 215506 (2005).

[67] L. Ventelon, F. Willaime, E. Clouet, and D. Rodney, Ab initio investigation of the Peierls potential of screw dislocations in bcc Fe and W, Acta Mater. **61**, 3973 (2013).

[68] L. Dezerald, L. Ventelon, E. Clouet, C. Denoual, D. Rodney, and F. Willaime, Ab initio modeling of the two-dimensional energy landscape of screw dislocations in bcc transition metals, Phys. Rev. B **89**, 024104 (2014).

[69] D. Caillard, Kinetics of dislocations in pure Fe. Part I. In situ straining experiments at room temperature, Acta Mater. **58**, 3493 (2010).

[70] M. R. Fellinger, A. M. Z. Tan, L. G. Hector, Jr., and D. R. Trinkle, Geometries of edge and mixed dislocations in bcc Fe from first-principles calculations, Phys. Rev. Mater. **2**, 113605 (2018).

[71] J. J. Möller, M. Mrovec, I. Bleskov, J. Neugebauer, T. Hammerschmidt, R. Drautz, C. Elsässer, T. Hickel, and E. Bitzek, {110} planar faults in strained bcc metals: Origins and implications of a commonly observed artifact of classical potentials, Phys. Rev. Mater. **2**, 093606 (2018).

[72] D. A. Smith and J. Gallot, Dissociated dislocations in iron observed by field-ion microscopy, Met. Sci. J. **3**, 79 (1969).

[73] J. J. Möller and E. Bitzek, Comparative study of embedded atom potentials for atomistic simulations of fracture in α-iron, Model. Simul. Mater. Sci. **22**, 045002 (2014).

[74] Y. Zhang, D. J. Yu, and K. M. Wang, Atomistic simulation of the orientation-dependent plastic deformation mechanisms of iron nanopillars, J. Mater. Sci. Technol. **28**, 164 (2012).

[75] Y. Yang, S. Z. Li, X. D. Ding, J. Sun, and E. K. H. Salje, Interface driven pseudo-elasticity in a-Fe nanowires, Adv. Funct. Mater. **26**, 760 (2016).

[76] J. Schiotz, F. D. Di Tolla, and K. W. Jacobsen, Softening of nanocrystalline metals at very small grain sizes, Nature (London) **391**, 561 (1998).

[77] V. Yamakov, D. Wolf, S. R. Phillpot, A. K. Mukherjee, and H. Gleiter, Deformation-mechanism map for nanocrystalline metals by molecular-dynamics simulation, Nat. Mater. **3**, 43 (2004).

[78] J. Inoue, A. Sadeghi, and T. Koseki, Slip band formation at free surface of lath martensite in low carbon steel, Acta Mater. **165**, 129 (2019).

[79] E. Chason, A. Engwall, F. Pei, M. Lafouresse, U. Bertocci, G. Stafford, J. A. Murphy, C. Lenihan, and D. N. Buckley, Understanding residual stress in electrodeposited Cu thin films, J. Electrochem. Soc. **160**, 3285 (2013).

[80] A. Hasnaoui, P. M. Derlet, and H. Van Swygenhoven, Interaction between dislocations and grain boundaries under an indenter - a molecular dynamics simulation, Acta Mater. **52**, 2251 (2004).

[81] Y. Shiihara, R. Kanazawa, D. Matsunaka, I. Lobzenko, T. Tsuru, M. Kohyama, and H. Mori, Artificial neural network molecular mechanics of iron grain boundaries, Scr. Mater. **207**, 114268 (2022).

[82] J. B. Yang, Y. Nagai, M. Hasegawa, and Y. N. Osetsky, Atomic scale modeling of {110} twist grain boundaries in α-iron: Structure and energy properties, Philos. Mag. **90**, 991 (2010).

[83] E. J. McEniry, T. Hickel, and J. Neugebauer, Hydrogen behaviour at twist {110} grain boundaries in α-Fe, Philos. Trans. R, Soc., A **375**, 2098 (2017).

[84] S. Ghosh, W. Z. Bao, D. L. Nika, S. Subrina, E. P. Pokatilov, C. N. Lau, and A. A. Balandin, Dimensional crossover of thermal transport in few-layer graphene, Nat. Mater. **9**, 555 (2010).

[85] Y. Zhou, J. Tranchida, Y. Ge, J. Murthy, and T. S. Fisher, Atomistic simulation of phonon and magnon thermal transport across the ferromagnetic-paramagnetic transition, Phys. Rev. B **101**, 224303 (2020).

[86] M. Sanati, R. C. Albers, T. Lookman, and A. Saxena, Elastic constants, phonon density of states, and thermal properties of UO, Phys. Rev. B **84**, 014116 (2011).

[87] B. N. Brockhouse, H. E. Abouhela, and E. D. Hallman, Lattice vibrations in iron at 296 degrees K, Solid State Commun. **5**, 211 (1967).

[88] H. C. Edwards, C. R. Trott, and D. Sunderland, Kokkos: Enabling manycore performance portability through polymorphic memory access patterns, J. Parallel Distrib. Comput. **74**, 3202 (2014).

[89] S. Plimpton, Computational limits of classical molecular-dynamics simulations, Comput. Mater. Sci. **4**, 361 (1995).

[90] S. Desai, S. T. Reeve, and J. F. Belak, Implementing a neural network interatomic model with performance portability for emerging exascale architectures, Comput. Phys. Commun. **270**, 108156 (2022).

[91] L. Yang, F. Zhang, C. Z. Wang, K. M. Ho, and A. Travesset, Implementation of metal-friendly EAM/FS-type semi-empirical potentials in HOOMD-blue: A GPU-accelerated molecular dynamics software, J. Comput. Phys. **359**, 352 (2018).

Correction: The previously published Figure 3 contained a typographical error in the legend and has been replaced.